The ZIMPOL high contrast imaging polarimeter for SPHERE: system test results

Ronald Roelfsema[*a], Andreas Bazzon[b], Hans Martin Schmid[b], Johan Pragt[a], Daniel Gisler[b], Carsten Dominik[c], Andrea Baruffolo[d], Jean-Luc Beuzit[e], Anne Costille[g], Kjetil Dohlen[g], Mark Downing[f], Eddy Elswijk[a], Menno de Haan[a], Norbert Hubin[f], Markus Kasper[f], Christoph Keller[h], Jean-Louis Lizon[f], David Mouillet[e], Alexey Pavlov[i], Pascal Puget[e], Bernardo Salasnich[d], Jean-Francois Sauvage[j], Francois Wildi[k]

a) NOVA Optical-Infrared Instrumentation Group at ASTRON, Oude Hoogeveensedijk 4, 7991 PD Dwingeloo, The Netherlands; b) Institute of Astronomy, ETH Zurich, 8093 Zurich, Switzerland; c) Astronomical Institute "Anton Pannekoek", 1098 SJ Amsterdam, The Netherlands; d) INAF, Osservatorio Astronomico di Padova, 35122 Padova, Italy; e) IPAG, Université Joseph Fourier, BP 53, 38041 Grenoble cedex 9, France; f) ESO, Karl-Schwarzschild-Strasse 2, D-85748 Garching bei München, Germany; g) LAM, UMR6110, CNRS/Universite de Provence, 13388 Marseille cedex 13, France; h) Leiden Observatory, Niels Bohrweg 2, P.O. Box 9513, 2300 RA Leiden, The Netherlands; i) Max-Planck-Institut fur Astronomie, Königstuhl 17, 69117 Heidelberg, Germany; j) ONERA, BP 72, 92322 Chatillon France;k) Observatoire Astronomique de l'Universite de Geneve, 1290 Sauverny, Switzerland;

ABSTRACT

SPHERE (Spectro-Polarimetric High-contrast Exoplanet Research) is a new instrument for the VLT aimed at the direct detection of exo-planets. It has received its first light in May 2014. ZIMPOL (Zurich Imaging Polarimeter) is the imaging polarimeter subsystem of the SPHERE instrument. It's capable of both high accuracy and high sensitivity polarimetry but can also be used as a classical imager. It is located behind an extreme AO system and a stellar coronagraph. ZIMPOL operates at visible wavelengths (600-900 nm) which is best suited to detect the very faint reflected and hence polarized visible light from extra solar planets. It has an instantaneous Field of View of 3 x 3 arcsec2 (extendable to 8 arcsec diameter) with an angular resolution of 14 mili-arcsec. We discuss the results that are obtained from the full SPHERE-ZIMPOL system testing. In particular the optical, polarimetric and high contrast performance.

Keywords: SPHERE, ZIMPOL, High Contrast, Exo Planets, Polarimetry, Adaptive Optics, Coronagraphy

1. INTRODUCTION

SPHERE-ZIMPOL[1][2][3] (Spectro-Polarimetric High Contrast Exoplanet Research - Zurich Imaging Polarimeter) is one of the first instruments which aim for the direct detection of reflected light from extra-solar planets. The instrument will search for direct light from old planets with orbital periods of a few months to a few years as we know them from our solar system. These are planets which are in or close to the habitable zone.

The reflected radiation is generally polarized [4][5] and the degree of polarization may be particularly high at short wavelengths < 1μm due to Rayleigh scattering by molecules and scattering by haze particles in planetary atmospheres. For this reason the visual-red spectral region is well suited for planet polarimetry.

*roelfsema@astron.nl; phone +31-(0)521-595172

The search for reflected light from extra-solar planets is very demanding, because the signal decreases rapidly with the orbital separation a. For a Jupiter-sized object and a separation of 1 AU the planet/star contrast to be achieved is on the order of 10^{-8} for a successful detection [6]. This is much more demanding than the direct imaging of young self-luminous planets. Therefore SPHERE-ZIMPOL will be capable to investigate only the very nearest stars for the polarization signal from extra-solar planets. There are half a dozen of good candidate systems for which giant planets should be detectable, even if their properties are not ideal (low albedo, not highly polarized). In another handful targets there is some chance to find high-polarization planets, if they exist around them. For stars further away a detection of reflected light with SPHERE-ZIMPOL will be difficult. At the present moment only three instruments at 8 meter class telescopes provide high angular resolution polarimetric capabilities in the near InfraRed: NAOS-CONICA[7] on the VLT, HiCIAO[8] on Subuaru and GPI[9] on Gemini South. SPHERE-ZIMPOL will be unique for providing high angular resolution polarimetry in the visible.

In this paper we present the high contrast polarimetric results obtained for the fully integrated SPHERE-ZIMPOL system in the lab in Grenoble, France. We describe the impact of crucial system parameters – coronagraphs, atmospheric conditions, spectral band and input polarization - on the contrast performance. Further we discuss several instrument effects that have impact on the polarimetric high contrast performance.

2. INSTRUMENT DESCRIPTION

2.1 SPHERE

ZIMPOL is one of the four sub-systems of SPHERE (see figure 1). The design of SPHERE is divided into four subsystems; the CPI[10] (Common Path and Infrastructure) and the three science channels: a differential imaging camera IRDIS[11] (Infrared Dual Imager and Spectrograph), an Integral Field Spectrograph (IFS)[12] and a visible imaging polarimeter (ZIMPOL). The instrument will be mounted to the Nasmyth platform rather than directly attached to the telescope Nasmyth rotator which is not adapted to carry the full charge of the instrument bench. All the sub-systems will be mounted onto a bench which is actively damped by a pneumatic servo-controlled system and equipped with a thermal cover. SPHERE is installed at the VLT and received first light in early May 2014.

ZIMPOL exploits a cascade of three techniques to achieve the required high contrast:

1) Extreme Adaptive Optics [14] to correct for turbulence induced by the Earth's atmosphere
2) Coronagraphy to remove the light of the central star
3) Polarimetry as differential technique to search for polarized planets in the residual light halo of the unpolarized star [13][16]

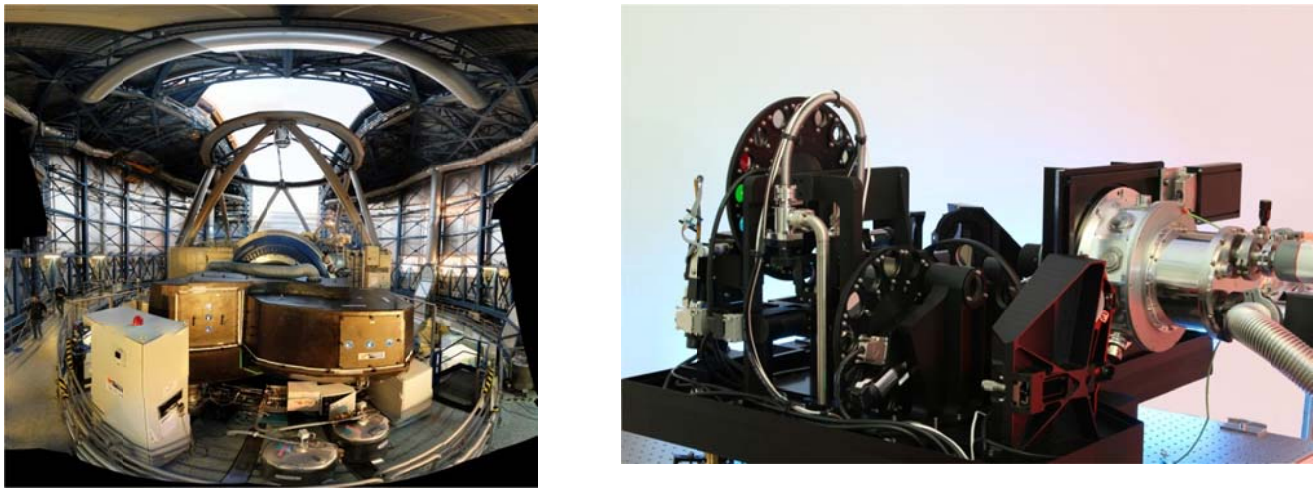

Figure 1 (left) SPHERE installed on the VLT UT3 - image J.F. Sauvage (right) The ZIMPOL high contrast polarimeter.

2.2 Coronagraphs

The basic concept of the ZIMPOL coronagraph is a combination of a set of broad band classical Lyot coronagraphs and two monochromatic Four Quadrant Phase Masks[15] (4QPM) which provide a smaller inner working angle. The inner working angles of the 3 λ/D and 5 λ/D Lyot coronagraphs are at 47 and 78 mas respectively. The Lyot Coronagraph mask radii are specified at 600 nm. The inner working angle of the 4QPM masks are expected to be around 20 mas.

The 5 λ/D Lyot mask in combination with broad band filters is foreseen to be the ZIMPOL main work horse for the initial planet detection given its robustness and photon collecting power. However, the planet contrast will improve rapidly with smaller star-planet separation and hence for follow up observation the coronagraphs with smaller working angle will be highly beneficial.

Table 1 SPHERE-ZIMPOL coronagraph configurations that have been used for our tests

Mask (ID)	Suspension	Field Stop	Lyot Stop Transmission (ID)
Lyot 3λ/D (CLC2)	Substrate	1 x 1 asec2	56 % (STOP2)
Lyot 5λ/D (CLC5)	Suspended	1 x 1 asec2	78 % (STOP1)
4Quadrant Phase Mask at 656 nm (4QPM1)	Substrate	8 arcsec diameter	73 % (STOP3)
4Quadrant Phase Mask at 820 nm (4QPM2)	Substrate	8 arcsec diameter	73 % (STOP3)

2.3 Spectral filters

ZIMPOL is equipped with several filter wheels: one common wheel and two non-common wheels in each arm. Among many other filters the common wheel contains several Neutral Density (ND) filters to control the flux levels. The ND-filters can be combined with the transmission filters in the non-common wheels. For our tests we have used the V (550/80), NR (655/60), NI (820/80) and VBB (750/290) filters where the numbers in brackets express the filter Central Wavelength/Bandwidth in nm.

2.4 Single Difference – FLC switch

The basic ZIMPOL principle [17] for high-precision polarization measurements includes a fast polarization modulator with a modulation frequency in the kHz range, combined with a CCD [17][18] detector which demodulates the intensity signal in synchronism with the polarization modulation. The modulation frequency is much faster than the seeing variations and therefore ZIMPOL is able to capture two subsequent images with nearly identical turbulent phase screens. The polarization modulator and associated polarizer convert the degree-of-polarization signal into a fractional modulation of the intensity signal which is then measured in a demodulating detector system by a differential intensity measurement between the two modulator states. Each active pixel measures both the high and the low states of the intensity modulation and dividing the differential signal by the average signal eliminates essentially all gain changes, notably changes of atmospheric transparency or electronic gain drifts.

2.5 Double Difference – HWP2 switch

By rotating a half-wave plate (HWP2) far upstream in the optical path by 45°, the sign of the incoming Stokes Q polarization is reversed. The instrumental aberrations, on the other hand, remain unchanged, resulting in the same background landscape as before. If the polarization images before and after the signal switching are subtracted from one another, the real polarization signals of the astronomical target add up constructively while the static background is canceled out.

2.6 Turbulence Simulator

A turbulence simulator is located at the optical entrance of the SPHERE bench. The turbulence is generated by a rotating phase screen [20]. For our tests we have used typical conditions of 0.85 arcsec seeing and 12.5 m/s windspeed that correspond to the 'normal' conditions that are foreseen at the VLT. The turbulence simulator is fed by a high energetic broad band source (Energetiq LDLS EQ-99FLC). This source produces a reasonable flat spectrum over the 500 – 790 nm band and has peaks at 820 and 880 nm.

2.7 Instrument Polarization

To achieve high contrast performance the polarized input signal at the ZIMPOL detectors must be lower than about 1%. Therefore we have characterized the polarimetric behaviour of the turbulence simulator and the SPHERE optical bench [21]. The polarization Q/I measured at the ZIMPOL detectors is a combination of polarization introduced before HWP2 (the Turbulence Simulator and mirror M4) and polarization introduced after HWP2 (the SPHERE optical components – in particular the derotator). To minimize the input polarization at the ZIMPOL detectors we have used a twofold strategy: 1) to minimize the input polarization introduced before HWP2 the HWP2 rotation is set at a Q/I zero crossing. The subsequent 45 degree HWP2 switch will also be at a zero crossing and 2) to minimize the input polarization introduced after HWP2 we have used the ZIMPOL internal Polarization Compensator.

3. DATA REDUCTION

The basic data reduction steps [24] are as follows. Bias is subtracted based on the pre –and overscan regions of the individual frames. The data is split in two datasets corresponding to the two HWP2 settings of the DD measurement. Each dataset is split up in sets of two consecutive frames and these sets are converted to Stokes Q taken into account the ZIMPOL CCD double phase mode operation. The Q frames are averaged and the end results are two final frames where each frame corresponds to a SD measurement. The two averaged SD frames are subtracted and divided by two to yield the final DD Stokes Q frame. An identical procedure is applied where the sets of two consecutive frames are converted to Stokes I taken into account the ZIMPOL double phase mode operation. This will yield the final DD Stokes I frame. From these two final DD frames it's obvious to obtain the overall normalized Stokes Q/I frame. The contrast is estimated from the noise level in the final averaged images. We will present our results as plots of azimuthal statistics as function of radial separation from the PSF peak. The azimuthal statistics are calculated over a ring with the width of a resolution element λ/D, i.e. 3 pixels.

4. PERFORMANCE MODELING

The ZIMPOL performance simulations are done with the CAOS [22] problem solving environment and are extensively described in Thalmann[23]. The model data that we present in this study is obtained with the same simulation code. Both the CAOS model data and the experimental data is processed by the same data reduction software to produce the standard contrast curves as shown in Figure 2. This figure is obtained with input parameters according to Standard Case 4 (SC4) as described by Thalmann[23] unless specified otherwise. We have used an integration time of about 1 hour to match the photon noise with our experimental data. The simulation of Figure 1 matches with our standard experimental test case:

- Coronagraph: Classical Lyot 5 λ/D
- Filter: NR
- Atmospheric conditions: Seeing 0.85 arcsec and wind speed 12.5 m/s
- Incoming polarization: Minimized

The results as of Figure 2 shown a standard diagram with the azimuthally averaged PSF Intensity signal or the rms-noise calculated for the corresponding azimuthal ring. The graphs include from the top to bottom:

- The azimuthally averaged non-coronagraphic PSF normalized to the peak signal. The azimuthal average is the mean of a ring with a width of a resolution element λ/D.

- The azimuthally averaged coronagraphic PSF normalized to the peak signal of the non-coronagraphic PSF. Averaging is done as above.
- The rms-noise level for the differential polarization signal. It is distinguished between the single-difference noise for HWP2 position 0 degrees and 45 degrees and the double difference noise when combining these two signals.
- The photon noise limit.

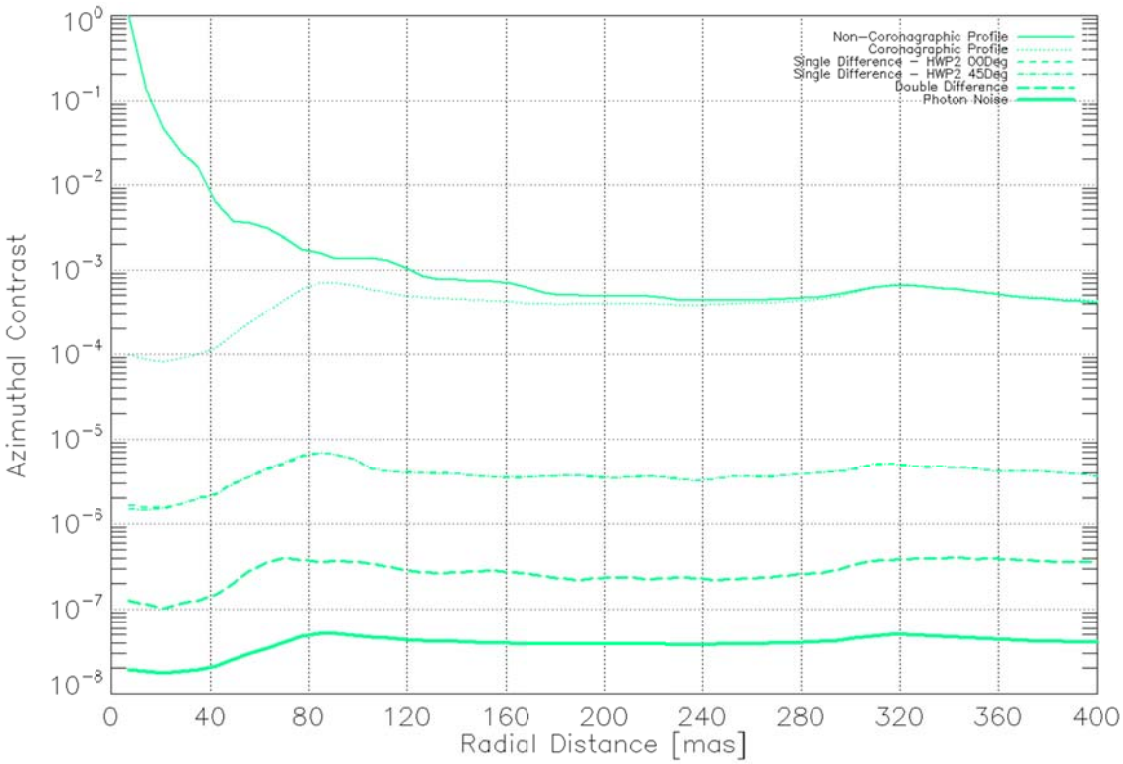

Figure 2 Simulated contrast curves from the CAOS model output of the standard test case using the input parameters of Standard Case4 (Thalmann[23]). Curves from top to bottom: non-coronagraphic profile, coronagraphic profile, Single Difference polarization for HWP2 at 00 and 45 deg, Double Difference polarization, photon noise limit. Confidence level 1-sigma.

5. HIGH CONTRAST PERFORMANCE MEASUREMENTS

This section describes the high contrast performance measurements done for SPHERE-ZIMPOL. First we describe the results of a standard test case. Subsequently we investigate the impact on the standard test case if we change a single parameter. The parameters under investigation are spectral filters, coronagraphs, atmospheric conditions and input polarization. Each test takes about 30 minutes and includes of the order of 1000 frames.

5.1 Standard test case

The standard setup for the high contrast tests is:

- Coronagraph: Classical Lyot 5 λ/D
- Filter: NR
- Atmospheric conditions: Seeing 0.85 arcsec and wind speed 12.5 m/s
- Incoming polarization: Minimized

The results of the standard test case are displayed in Figure 3 and the contrast curves are shown in Figure 4.

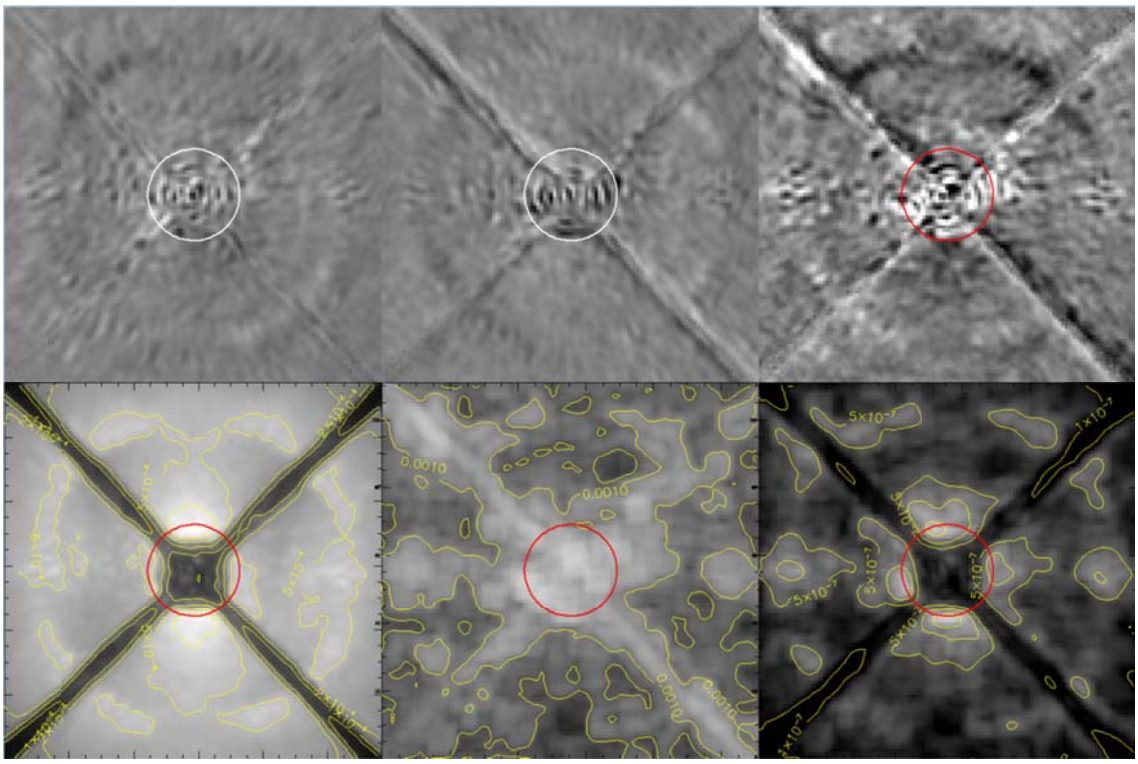

Figure 3 Measured images for the standard test case. Images: top row from left to right: single difference polarization HWP2 at 0 degrees, at 45 degrees and double difference combing the two. (bottom left) normalized coronagraphic PSF, (middle) polarimetric noise and (right) contrast. The radius of the circle is 100 mas.

The comparison of the simulated (Figure 2) and measured (Figure 4) test curve reveal the following points:

- The measured coronagraphic PSF profile matches very well with the simulated curves.
- The measured SD contrast curves (1×10^{-6} at 240 mas) are about a factor of 3 better than predicted by the simulations (3×10^{-6} at 240 mas)
- The measured DD contrast (8×10^{-7} at 200 mas) is about 4 times lower than predicted by the simulations (2×10^{-7} at 200 mas)
- The double difference (HWP2 switch) provides in the simulation an additional gain contrast of about a factor of 10 (Figure 2). The measurement results show only a small improvement here, perhaps by a factor 2. It seems that the HWP2 switch does not help as much as expected.

We have investigated the latter issue in more detail and we concluded that small beamshift effects seem to dominate the noise performance of SPHERE-ZIMPOL. Beamshift measurements on various components of the SPHERE-ZIMPOL system reveal the following shifts as measured on the ZIMPOL detectors:

HWP2	0.05 pix	when switched over 45 degrees
Derotator	0.1 pix	when rotated over 90 degrees
FLC	0.01 pix	when switched between two states

Especially the beamshifts from HWP2 and the derotator are much higher than anticipated. In principle we should expect that pure beamshifts can be taken into account in the data processing, i.e. measuring the beamshifts and correcting for the beamshift before the frame combination. However, if we do so we only achieve a modest contrast improvement of about 10 – 30 %.

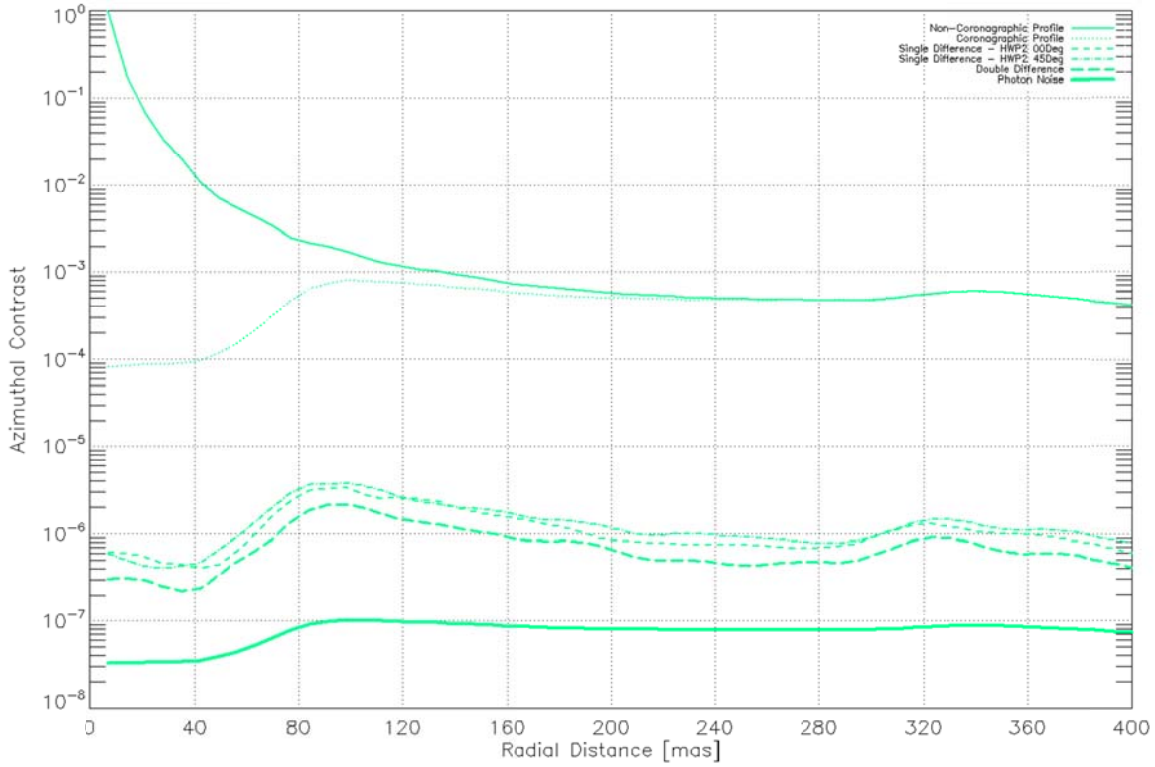

Figure 4 Measured contrast curves for the standard test case. Curves from top to bottom: non-coronagraphic profile, coronagraphic profile, Single Difference polarization for HWP2 at 00 and 45 deg, Double Difference polarization, photon noise limit. Confidence level 1-sigma.

To find a better correspondence between the measurements and the simulations we have adjusted two groups of input parameters of the CAOS model and kept the rest of the input parameters as of the Standard Case4[23]. The adjusted parameters as listed in Table 2 only have impact on the pre-coronagraph differential and post coronagraph differential wave front errors.

Table 2 Input parameters for the CAOS performance simulation.

	Standard Case4	Adjusted to
CPI differential beam shift (nm)	0	30
ZIM phase differential aberration (nm)	0.75	0.25
ZIM pointing differential aberration (nm)	0.75	0
ZIM beamshift effect (nm)	0.75	0

The resulting simulation is shown in Figure 5 and we conclude a good match with Figure 4. We see that by reducing the ZIMPOL differential aberration the SD performance is improved whereas the increase of the CPI differential aberrations reduces the gain in DD performance.

We must remark that in the current stage the adjusted numbers can only be considered as 'fitting' parameters to match the simulations with the measurements. If we convert the measured beamshifts (Δx) to wavefront errors (Δw) according to $\Delta w = \Delta x/(2F)$ where F = 221 the F-number at the ZIMPOL detector we arrive at 1.5 nm for the ZIM differential aberration and at about 15 nm for the CPI differential aberration, i.e. values that differ significantly from the adjusted input parameters. Therefore we conclude that other mechanisms then pure differential aberrations are causing the ZIMPOL performance degradation.

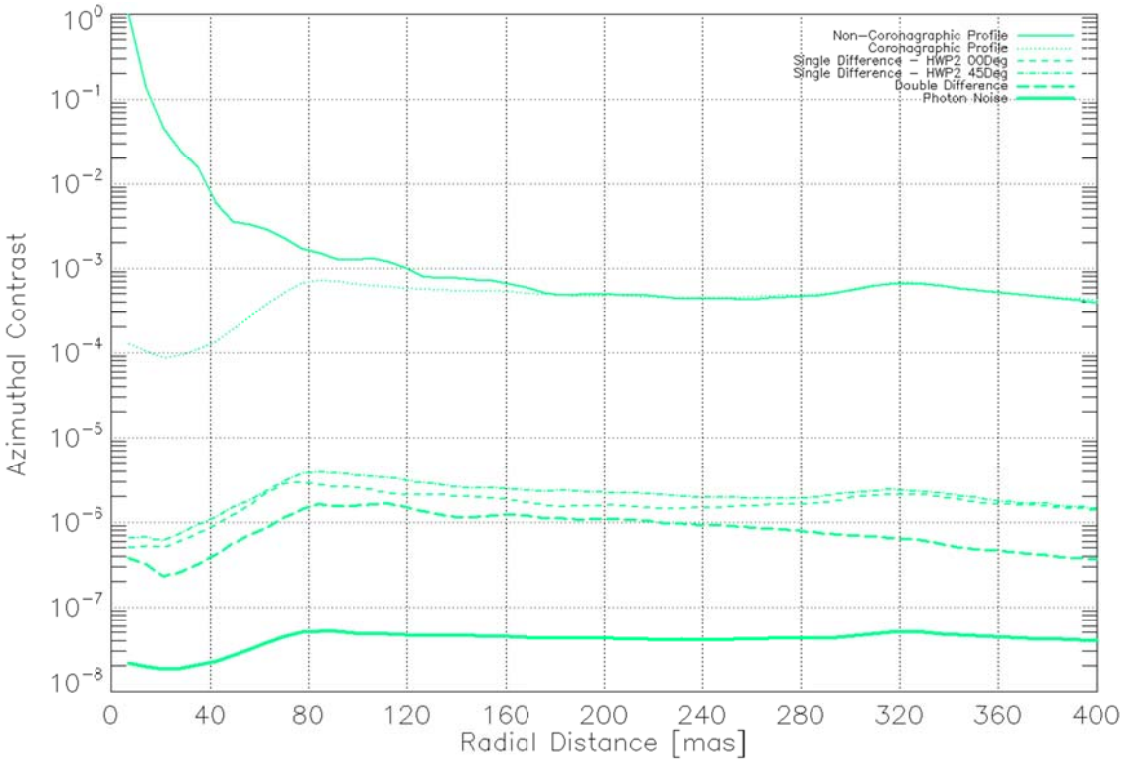

Figure 5 Simulated contrast curves from the CAOS model output of the standard test case using the input parameters of Standard Case4 with adjusted input parameters as of Table 2 . Curves from top to bottom: non-coronagraphic profile, coronagraphic profile, Single Difference polarization for HWP2 at 00 and 45 deg, Double Difference polarization, photon noise limit. Confidence level 1-sigma.

5.2 Spectral filters

Measurements as of the standard test case but for different color filters were carried out. Figure 6 shows the contrast plots for the shorter wavelength in the V filter and in the longer wavelength in the NI filter.

As expected the AO and coronagraphic performance is better for longer wavelength. This is particularly well visible for a radius beyond 120 mas where the coronagraphic performance is about a factor of 3 better in the I-band. However, at the same time the differential polarimetry works better at short wavelengths so that in the end the overall contrast performance is comparable for the two wavelengths. We have measured the contrast at a separation of 240 mas and obtain for filters, V, NR, and NI the same limit of 4×10^{-7}.

That polarimetry works better at short wavelength is an interesting result and is illustrated by the Double Difference polarization images in Figure 7. The images show that the NI-band differential polarization signal is much more affected

by residual speckles and diffraction effects. Thus the lower AO and coronagraph performance at short wavelengths is compensated by the improved polarimetry.

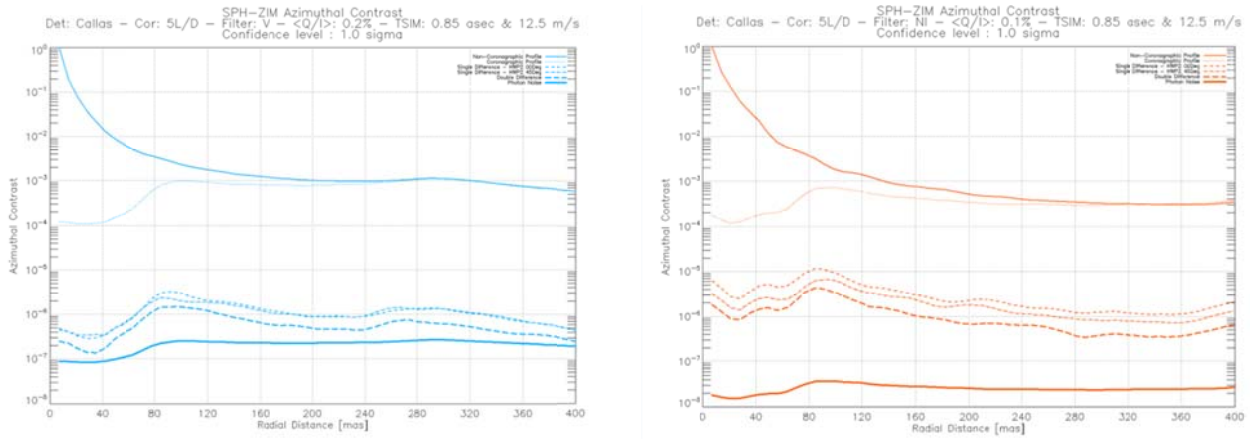

Figure 6 Comparison of the measured PSF and contrast curves for the standard test case with V-filter (left) and the NI-filter (right). Curves from top to bottom: non-coronagraphic profile, coronagraphic profile, Single Difference polarization for HWP2 at 00 and 45 deg, Double Difference polarization, photon noise limit.

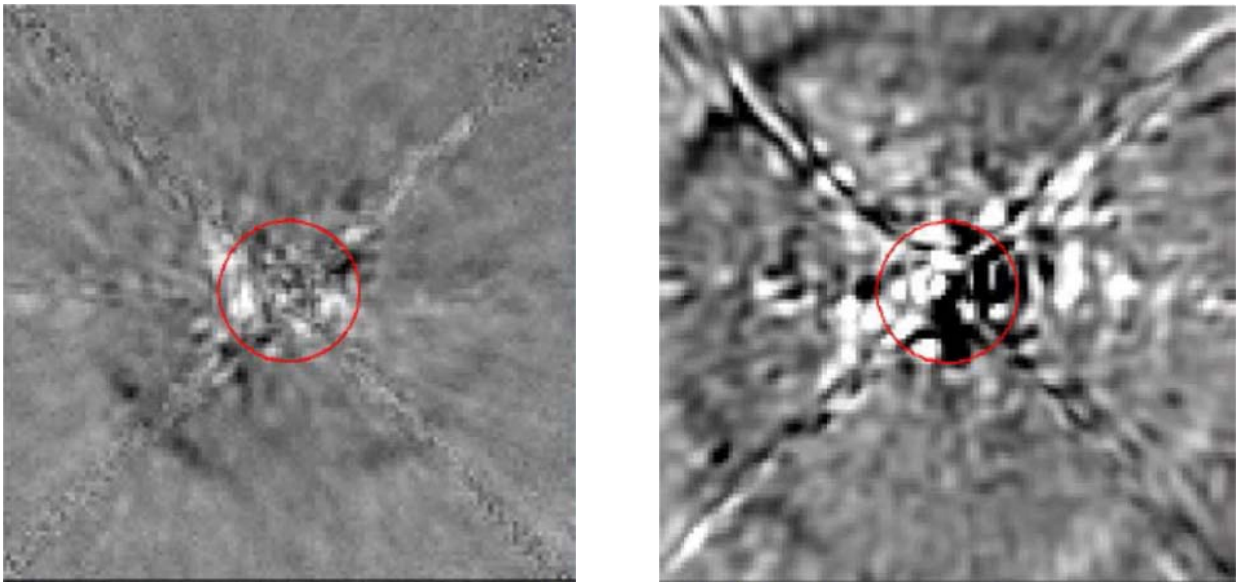

Figure 7 Measured images for DD-polarization for V-filter (left) and NI-filter (right). The radius of the circle is 100 mas.

5.3 Coronagraphs

Measurements as of the standard test case but with different coronagraphs were made. The standard curves are displayed in Figure 8. We concentrate here on the difference of the smaller 3λ/D-Lyot mask and the 4QPM1 with respect to the standard test case taken with the 5λ/D-standard mask.

Both coronagraphs have outside a radius of 100 mas approximately the same PSF profiles as the standard 5λ/D masks. The 3 λ/D coronagraph and the 4QPM1 provide significantly smaller inner working angles of about 55 mas for the 3 λ/D

mask and as low as perhaps 25 mas for the 4 QPM1 (IWA for the 5 λ/D mask is about 90 mas). The peak flux of the 4QPM1 in the center is only about 30 times higher than at 100 mas and this should not cause severe problems with detector saturation.

To investigate the residual speckle and diffraction effects close to the PSF core in more detail we have done test with the 4QPM2 coronagraph in the NI-band. We expect these effects to be most pronounced for this case. The SD and DD polarization images obtained with the 4QPM2 in NI-band are shown in Figure 9. In the SD images we see a distinct polarized ring pattern. Unfortunately we also see in the figure that this pattern also survives the DD-subtraction and causes relatively high noise levels. This is particular harmful close to the PSF core where polarimetric planet detection is most favorable.

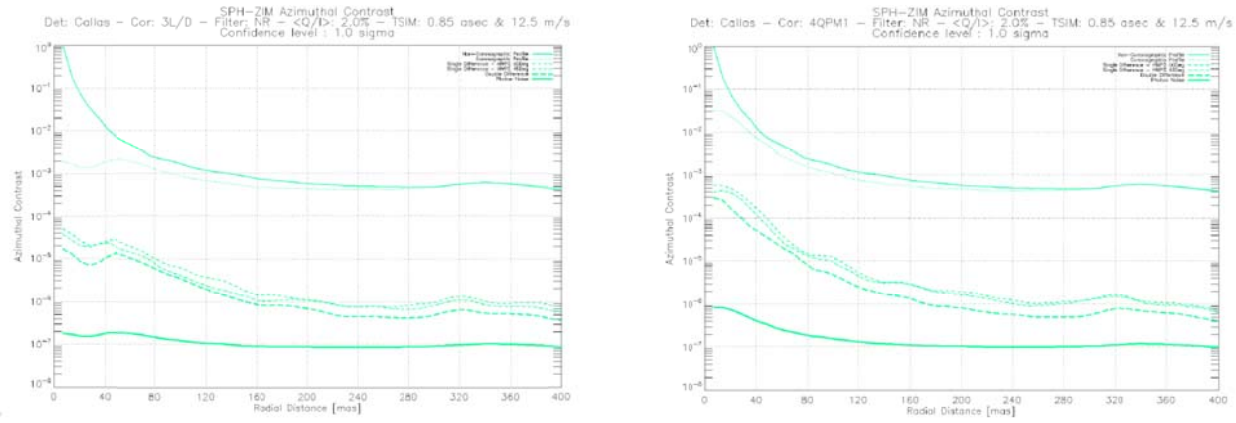

Figure 8 Comparison of the PSF and contrast curves for the 3λ/D mask (left) and the 4QPM1 (right) in the NR band. Curves from top to bottom: non-coronagraphic profile, coronagraphic profile, Single Difference polarization for HWP2 at 00 and 45 deg, Double Difference polarization, photon noise limit.

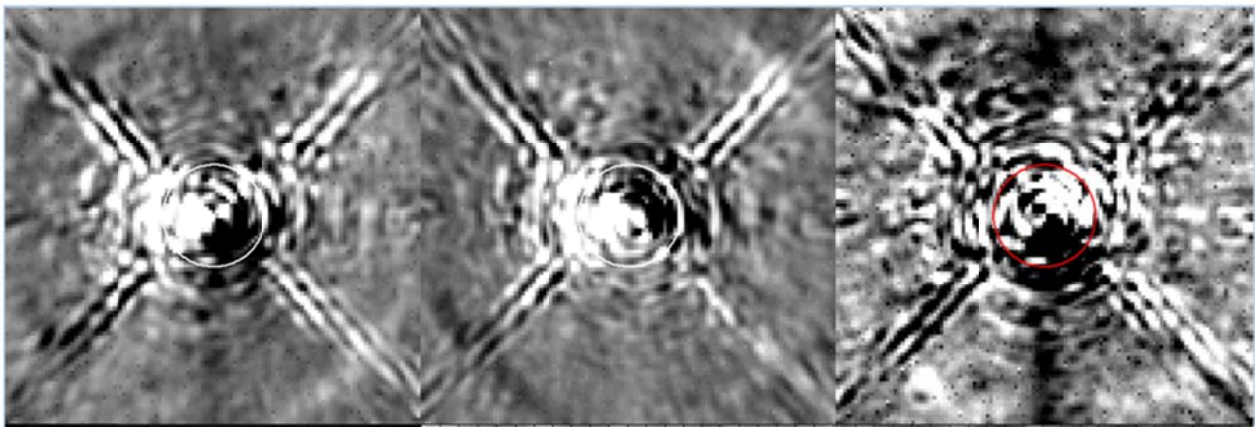

Figure 9 Measured polarization images for 4QOM2 with NI-filter from left to right: single difference polarization HWP2 at 0 degrees, at 45 degrees and double difference combing the two SD images. In the two SD images we see a polarized ring pattern close to the PSF core. This ring pattern doesn't completely subtract out as can be seen in the DD-image. The radius of the circle is 100 mas.

5.4 Atmospheric conditions

Measurements as of the standard test case but for different atmospheric conditions were made. We carried out test with the turbulence simulator for 3 different wind speeds. They represent, besides the average condition with a seeing of 0.85

arcsec and average wind speed of 12.5 m/s, poor conditions with a wind speed of 37.5 m/s and good conditions with a wind speed of 6.3 m/s. The standard curves are displayed in Figure 10. As expected the atmospheric turbulence has a signifcant impact on the high contrast performance. The AO performance is significantly better for good conditions by about a factor of 10. The difference in the final polarimetric contrast is in the end about a factor of 4. Particularly interesting is that the difference occurs mainly between the poor and medium conditions while there is hardly a difference in polarimetric contrast performance between medium and good conditions. This suggests that one should not seek for particularly good atmospheric conditions for high contrast imaging with ZIMPOL. This statement must of course be confirmed with real on-sky observations.

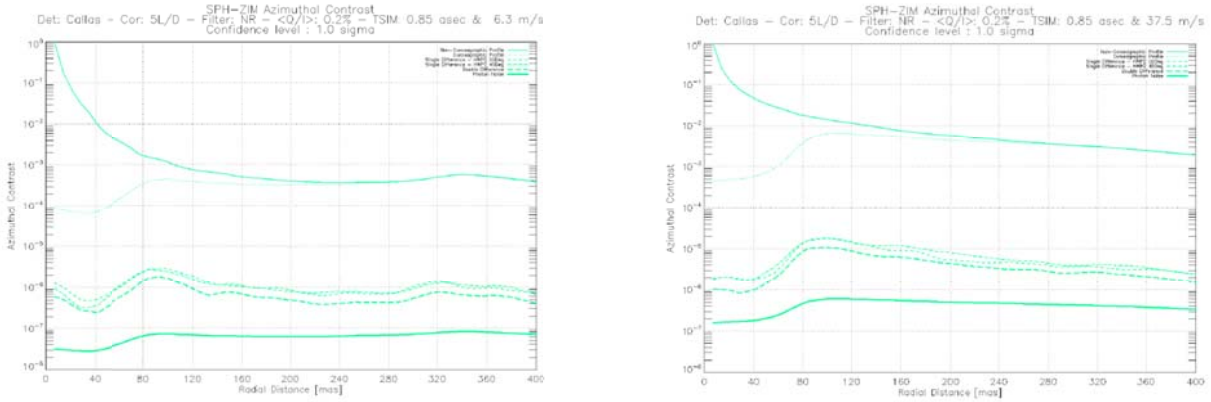

Figure 10 Comparison of the PSF and contrast curves for low wind speed (left) and high wind speed (right) in the NR band. Curves from top to bottom: non-coronagraphic profile, coronagraphic profile, Single Difference polarization for HWP2 at 00 and 45 deg, Double Difference polarization, photon noise limit.

The reason for the relatively small difference between the bad and medium conditions is similar to the case for measurements for different wavelengths. If the AO performance is good then the PSF is less smeared and shows more speckles which reduces the polarimetric performance because of the larger impact of beam shift effect for strong gradients. This is illustrated in Figure 11 that shows noise in the final Double Difference polarization image for poor and good atmospheric conditions.

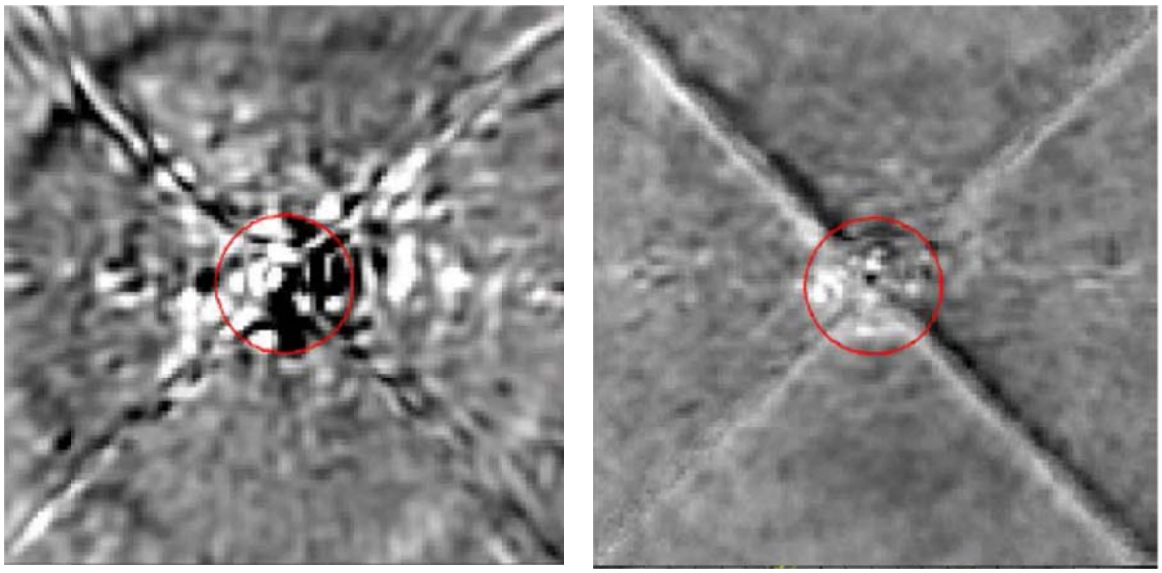

Figure 11 Measured images for DD-polarization for good atmospheric conditions (left) and poor atmospheric conditions (right). The radius of the circle is 100 mas.

5.5 Input polarization

One could imagine that the performance is reduced if the overall polarization of the incoming star light is polarized by interstellar matter or the telescope. With flat field illuminations free of strong intensity gradients it was demonstrated that highest sensitivity of 10-5 could only be achieved if the polarization of the illumination was less than about 1%[24].

Measurements as of the standard test case but with different levels of input polarization were made. The limited performance of the standard test case is not caused by the polarization of the illuminating point source. We have checked this with high contrast tests inducing for the incoming light a high polarization of 3.2%. The measured double difference noise performance was not affected by this when compared to very low polarized (<0.2%) incoming light. One reason for not seeing an effect is that the polarimetric sensitivity is reduced in the high contrast tests due to the beam-shift effect acting on the speckle pattern of the PSF. Thus the effect of the polarized incoming light seems to be too small to be noticed in the high contrast data. We conclude that instrumental polarization is not critical, unless the polarimetric contrast can be further enhanced toward the previously anticipated goal value.

6. DISCUSSION

The high contrast measurement data as presented in the previous section strongly indicates that complex beamshifts effects have a strong impact on the SPHERE-ZIMPOL performance. In this section we will discuss several components that will introduce beam deviations between the two orthogonal linear polarization states in the optical path.

6.1 HWP2 beamshifts

In the SPHERE-ZIMPOL system we observe that HWP2 introduces a beamshift on the ZIMPOL CCDs of about 0.1 pixel where 1 pixel has a size of 60×60 micron. We can attribute this beamshift to a cutting error of the HWP2 crystal, i.e. the crystal is not cut exactly parallel to the crystal optical axis. The dispersion angle α between the e –and o-beam is then given by

$$\tan(\alpha) = \frac{(n_e^2 - n_o^2)\tan(\Delta\theta)}{n_e^2 + n_o^2 tan^2(\Delta\theta)}$$

where Δθ is the cutting error and n_e = 1.55051 and n_o = 1.54148 for Crystal Quartz at 670 nm. In the SPHERE-ZIMPOL optical system HWP2 is located 187 mm from the F/15 VLT input focal plane. The focal ratio of the camera lens on the ZIMPOL CCD is F/221. An angular beam deviation at the location of HWP2 will hence be magnified as a beam displacement on the ZIMPOL CCD by a factor of 187×(221/15) = 2755.

We calculate that a beamshift of 0.1 pixel is caused by a cutting error of only 0.01 deg (36 asec). From a manufacturing point of view this seems like an excellent achievement. However, the location of HWP2 in the SPHERE optical setup magnifies the beam deviation by a factor of 2755.

6.2 FLC beamshifts

In the SPHERE-ZIMPOL system we observe that the FLC introduces a beamshift at the ZIMPOL CCDs of about 0.01 pixel where 1 pixel has a size of 60×60 micron. The FLC consists of a thin layer of liquid crystals confined between two relatively thick and stiff fused silica substrates. Small glass spheres are used as spacers between the substrates to achieve a gap of about 3 micron thickness. We assume that the beamshift is caused by a small wedge angle in the liquid crystal gap. To estimate the wedge angle we proceed as follows.

The beamshift of 0.01 pixel on the ZIMPOL CCD corresponds to about 1 micron. The FLC is located in a collimated beam just in front of the ZIMPOL camera lens with a focal length of about 1400 mm. Therefore the angular beam deviation introduced by the FLC will be about $(1\times10^{-3})/1400 = 7\times10^{-7}$ radians and the wedge angle $\gamma = (7\times10^{-7})/\Delta n = 6.5\times10^{-6}$ radians ~ 1 arcsec. The FLC diameter is about 25 mm and so the error in the spherical spacers is in the order of $25 \times 6.5\times10^{-6} \sim 0.15$ micron.

From a manufacturing point of view this seems a very good achievement. However, we see that in the ZIMPOL optical system the small differential tilt will be levered by a factor of 1400 to show up as a beamshift on the ZIMPOL CCDs.

6.3 Polarized ring structure

Fabry Perot[26](FP) effects in the FLC[25] can cause a residual ring structure in the polarization signal as observed in Figure 9 and hence a residual noise pattern.

The FLC contains a (very accurate) parallel gap between two substrate filled with liquid crystals. The inside of the two substrate plates are coated with an ITO (Indium Tin Oxide) coating to serve as electrodes. The reflectance of the ITO coating is relatively high compared to standard anti-reflection coatings. The FLC gap and reflective ITO coatings act as FP etalon. Moreover, switching of the FLC will change the index of refraction of the gap and will therefore induce a change in the FP transmission profile (see Figure 12).

The PSF can be calculated as an integral over the spectral band of a mono-chromatic Airy pattern weighted with the even and odd transmission profiles. This gives slightly different PSFe and PSFo profiles for the two FLC switching states and hence ring shaped residuals will show up in the polarized image given by (PSFe-PSFo)/(PSFe+PSFo) as can be seen in Figure 12.

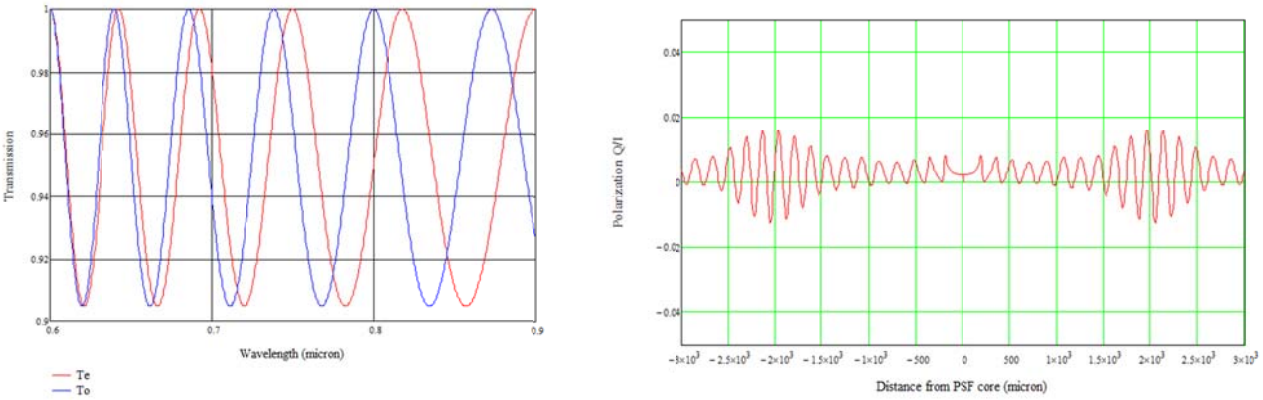

Figure 12 (right) Fabry Perot effects in the FLC transmission profiles for the two FLC switching states (right) Residual SD polarization signal

An FP-etalon might be sensitive to the angle of incidence. This means that beam shift effects that are caused upstream might have impact on FP output pattern and thereby on the polarization pattern. However, the observed beam shift effects are so small that they can't give rise to differences in the two SD images, i.e. the tilt angles in the FLC cavity lead to differential optical path lengths orders of magnitude smaller than the wavelength. In other words, the FP pattern in both SD images is nearly similar and will subtract in the DD. Since this is not the case we conclude that FP effects are not the main cause of the performance degradation.

6.4 Metallic mirror beamshifts

The observed beamshifts for the derotator are attributed to the small spatial and angular deviations from specular reflection. Such deviations are classified as Goos-Hanchen[27] (GH) effect for a linear polarized input beam and as Imbert-Federov[28] (IF) effect for a circular polarized input beam (see Figure 13 copied from Merano[30]). The Goos-Hanchen beam deviations occur in the plane of incidence whereas the Imbert-Federov deviations are normal to the plane of incidence. In the context of SPHERE-ZIMPOL beam deviations to first order we are only concerned with linear polarization and therefore we will only concentrate on the Goos-Hanchen effect.

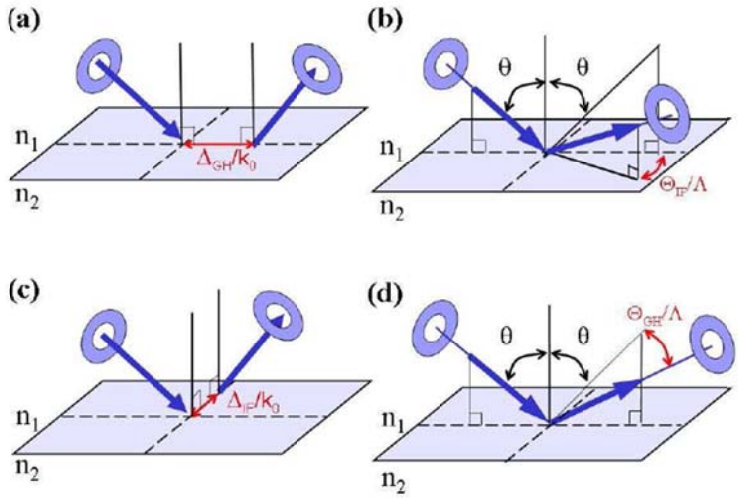

Figure 13 Polarized beamshifts effects in metallic mirrors. Panel (a) shows the spatial Goos-Hanchen effect, panel (b) the angular Imbert-Fedorov effect, panel (c) the spatial Imbert-Fedorov effect and panel (d) the angular Goos-Hanchen effect. Copied from Merano[30].

To calculate the spatial and angular Goos-Hanchen displacements we follow the approach as outlined by Aiello[29]. The spatial (Δ) and angular (Θ) GH-displacements are given by

$$\Delta_{p,s} = \frac{2\pi}{\lambda}\,\mathrm{Im}\left(D_{p,s}\right) \qquad \Theta_{p,s} = \frac{-1}{2}(\theta_o)^2\,\mathrm{Re}\left(D_{p,s}\right)$$

where θo is the beam diverging angle and the subscript p,s indicate the p- and s-polarization directions. For SPHERE-ZIMPOL we replace this expression by the beam opening angle according to the F-number of the optical system

$$\theta_o = \frac{1}{2F}$$

The quantity $D_{p,s}$ is given by

$$D_{p,s} = \frac{\partial \ln(r_{p,s})}{\partial\theta} = \frac{1}{r_{p,s}}\frac{\partial r_{p,s}}{\partial\theta}$$

where θ is the angle of incidence and $r_{p,s}$ are the Fresnel reflection coefficients with complex index of refraction given by

$$r_p = \frac{\tilde{n}^2\cos(\theta) - \sqrt{\tilde{n}^2 - sin^2(\theta)}}{\tilde{n}^2\cos(\theta) + \sqrt{\tilde{n}^2 - sin^2(\theta)}} \qquad r_s = \frac{\cos(\theta) - \sqrt{\tilde{n}^2 - sin^2(\theta)}}{\cos(\theta) + \sqrt{\tilde{n}^2 - sin^2(\theta)}}$$

These equations assume an air-metal interface where the index of refraction of air is unity and the complex index of the metal is given by

$$\tilde{n} = n - ik$$

For a first estimate we assume a silver coating for the optics. We trace the beam deviations to the ZIMPOL detectors according to

$$Spatial\_Shift = 2\left(\frac{1}{pix}\right)\left(\frac{221}{15}\right)(\Delta_p - \Delta_s)$$

$$Angular\_Shift = 2L\left(\frac{1}{pix}\right)\left(\frac{221}{15}\right)(\Theta_p - \Theta_s)$$

where pix = 60 micron, the factor of 2 comes from two derotator mirrors at 55 deg angle of incidence, (221/15) is the ratio of F-numbers at the ZIMPOL camera and the derotator, L = 350 mm which is about the average distance from the derotator to the F/15 VLT-focus. The results are shown in Figure 14.

It seems that the calculated values for the spatial beamshift correspond very reasonable with the measured values of an overall beamshift of 0.1 pixels. However, the model predicts angular beamshifts that are much larger than the measured values. The probable cause for this deviation is that the he layered structure of the derotator coating is much more complex than can be described by the wavelength dependent index of refraction of silver.

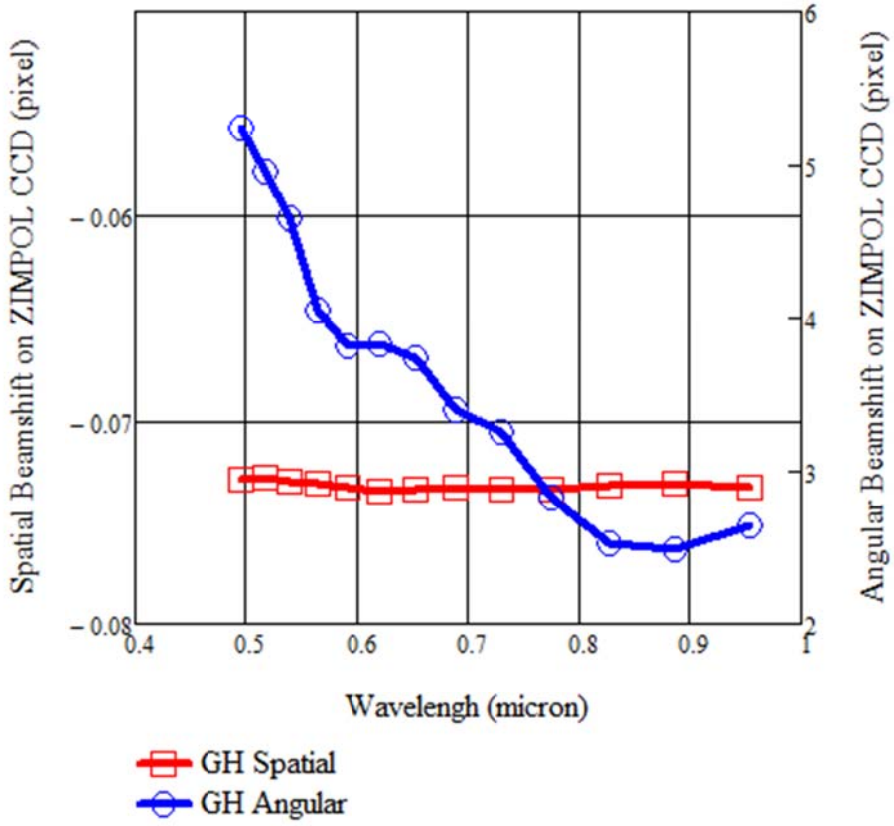

Figure 14 Estimated beam shifts at the ZIMPOL detector as caused by the Goos-Hanchen spatial (red) and angular (blue) deviations.

6.5 Future work

Currently we are working on a system model that assumes that what we see on the detector is not pure beamshift effect. Some components (HWP2, derotator, FLC) will split the unpolarized input beam in orthogonal polarized sub-beams. Components further downstream will again split a single sub-beam in two other sub-sub beams. So on the detector we see some superposition of sub-beams where each sub-beam is slightly displaced w.r.t. the other sub-beams and each sub-beam might have different amplitude then the other sub-beams. In general the first element splits the beam in two sub-beams, the second element splits the beam in four sub-beams, the third element splits the beam in eight sub-beams, etc. This would also explain why correcting for the beam shift only gives rather modest performance improvement. We assume that unpolarized input beam splits in many sub-beams and that the residual noise pattern is caused by superposition of sub-beams. We are working on component and system improvements and will use the model to quantify the impact on high contrast performance.

7. CONCLUSIONS

The SPHERE-ZIMPOL high contrast tests carried out in September 2013 at IPAG, Grenoble, France give a good assessment of the polarimetric contrast performance of ZIMPOL including the AO and coronagraph performance.

We have demonstrated with realistic system tests that ZIMPOL reaches a contrast better than 10^{-6} using the foreseen polarimetric double-difference technique. This is at least one order of magnitude better than any previous high contrast polarimetry published today. However, the performance is about a factor four less good than expected because of unforeseen instrumental effects.

Of particular interest is that the polarimetric performance is better if the AO performance is less good and vice versa. Speckle subtraction by polarimetry suffers mainly by the beam shift effects that are currently under investigation. Improvements in the correction or calibration of the beam shift effect will in particular help to push the performance for observations taken under very good AO conditions, long wavelengths and good seeing because these observations are most affected by the residual speckle pattern.

Using angular differential imaging techniques [31] at the telescope it should be possible to push the polarimetric contrast limits towards 1×10^{-7} which would be reachable from day one. It is not excluded that improved data reduction based on further analysis of the instrument, upgrades of individual components, or more sophisticated observing strategies can provide in the near future the goal performance contrast of 10^{-8} for SPHERE-ZIMPOL. However it seems now too optimistic to hope for such a performance already during the first year(s) of operation of the instrument.

REFERENCES

[1] Schmid, H. M., Beuzit, J.-L., Feldt, M., Gisler, D., Gratton, R., Henning, T., Joos, F., Kasper, M., Lenzen, R., Mouillet, D., Moutou, C., Quirrenbach, A., Stam, D. M., Thalmann, C., Tinbergen, J., Verinaud, C., Waters, R., and Wolstencroft, R., "Search and investigation of extra-solar planets with polarimetry," IAU Colloq. 200, 165–170 (2006)

[2] D. Gisler, H.M. Schmid, C. Thalmann, H.P. Povel, J.O. Stenflo, F. Joos, M. Feldt, R. Lenzen, J. Tinbergen, R. Gratton, R. Stuik, D.M. Stam, W. Brandner, S. Hippler, M. Turatto, R. Neuhäuser, C. Dominik, A. Hatzes, Th. Henning, J. Lima, A. Quirrenbach, L.B.F.M. Waters, G. Wuchterl, H. Zinnecker, "CHEOPS/ZIMPOL: a VLT instrument study for the polarimetric search of scattered light from extrasolar planets," Proc. SPIE 5492, 463-474 (2004)

[3] Beuzit, J.-L., Feldt, M., Dohlen, K., Mouillet, D., Puget, P., Antichi, J., Baruffolo, A., Baudoz, P., Berton, A., Boccaletti, A., Carbillet, M., Charton, J., Claudi, R., Downing, M., Feautrier, P., Fedrigo, E., Fusco, T., Gratton, R., Hubin, N., Kasper, M., Langlois, M., Moutou, C., Mugnier, L., Pragt, J., Rabou, P., Saisse, M., Schmid, H. M., Stadler, E., Turrato, M., Udry, S., Waters, R., and Wildi, F., "SPHERE: A 'Planet Finder' Instrument for the VLT," The Messenger 125, 29–34 (2006)

[4] D. M. Stam, "Spectropolarimetric signatures of Earth-like extrasolar planets," A&A 482, 989-1007 (2008)

[5] E. Buenzli, H.M. Schmid, “A grid of polarization models for Rayleigh scattering planetary atmospheres,” Astron. Astrophys. 504, 259-276 (2009)
[6] Julien Milli, David Mouillet, Dimitri Mawet, Hans Martin Schmid, Andreas Bazzon, Julien H. Girard, Kjetil Dohlen, Ronald Roelfsema, “Prospects of detecting the polarimetric signature of the Earth-mass planet alpha Centauri B b with SPHERE / ZIMPOL,” A&A, (2013)
[7] Sascha P. Quanz, Hans Martin Schmid, Kerstin Geissler, Michael R. Meyer, Thomas Henning, Wolfgang Brandner, Sebastian Wolf, “VLT/NACO Polarimetric Differential Imaging of HD100546 - Disk Structure and Dust Grain Properties between 10-140 AU,” ApJ, 738 Issue 1, 23 (2011)
[8] Michihiro Takami et al, “High-Contrast Near-Infrared Imaging Polarimetry of the Protoplanetary Disk around RY Tau,” ApJ 772, Issue 2, 145 (2013)
[9] Macintosh, B., Graham, J. R., Ingraham, P. et al, “The Gemini Planet Imager: First Light,” ArXiv e-prints 1403.7520 (2014)
[10] Jean-François Sauvage, Jean-Luc Beuzit, Ronald roelfsema, et al., "Sphere: complete laboratory performance and prediction for on-sky first light", Proceedings of SPIE Vol. 8864, 88640B (2013)
[11] Kjetil Dohlen , Michel Saisse et al, “Manufacturing and integration of the IRDIS dual imaging camera and spectrograph for SPHERE,” Proc. SPIE 7735, (2010)
[12] Ricardo Claudi, “SPHERE IFS: The spectro differential imager of the VLT for exoplanets search,” Proc. SPIE 7735, (2010)
[13] Franco Joos, Esther Buenzli, Hans Martin Schmid and Christian Thalmann, “Reduction of polarimetric data using Mueller calculus applied to Nasmyth instruments,“ Proc. SPIE 7016, (2008)
[14] C. Petit , J.-F. Sauvage , A. Sevin ; A. Costille , T. Fusco , P. Baudoz , J.-L. Beuzit , T. Buey , J. Charton , K. Dohlen , P. Feautrier , E. Fedrigo , J.-L. Gach , N. Hubin , E. Hugot , M. Kasper , D. Mouillet , D. Perret , P. Puget , J.-C. Sinquin , C. Soenke , M. Suarez , F. Wildi, “The SPHERE XAO system SAXO: integration, test, and laboratory performance,” Proc. SPIE 8447, (2012)
[15] Rouan, D., Riaud, P., Boccaletti, A., Cl´enet, Y., and Labeyrie, A., “The Four-Quadrant Phase-MaskCoronagraph. I. Principle,” The Publications of the Astronomical Society of the Pacific 112, 1479–1486 (2000)
[16] Quanz, Sascha P.; Meyer, Michael R.; Kenworthy, Matthew A.; Girard, Julien H. V.; Kasper, Markus; Lagrange, Anne-Marie; Apai, Daniel; Boccaletti, Anthony; Bonnefoy, Mickaël; Chauvin, Gael; Hinz, Philip M.; Lenzen, Rainer, “First Results from Very Large Telescope NACO Apodizing Phase Plate: 4 μm Images of The Exoplanet β Pictoris b,” ApJ 722, 49 (2010)
[17] Povel, H. P., Aebersold, F., and Stenflo, J., “Charge-coupled device image sensor as a demodulator in a 2-D polarimeter with a piezoelastic modulator,” Appl. Opt. 29, 1186 (1990)
[18] Schmid, Hans-Martin; Downing, Mark; Roelfsema, Ronald; Bazzon, Andreas; Gisler, Daniel; Pragt, Johan; Cumani, Claudio; Salasnich, Bernardo; Pavlov, Alexey; Baruffolo, Andrea; Beuzit, Jean-Luc; Costille, Anne; Deiries, Sebastian; Dohlen, Kjetil; Dominik, Carsten; Elswijk, Eddy; Feldt, Markus; Kasper, Markus; Mouillet, David; Thalmann, Christian; Wildi, François, “Tests of the demodulating CCDs for the SPHERE / ZIMPOL imaging polarimeter,” Proc. SPIE 8446, (2012)
[19] P. Martinez, C. Loose, E. Aller Carpentier and M. Kasper, “Speckle temporal stability in XAO coronagraphic images,” A&A 541, A136 (2012)
[20] L. Jolissaint, “Optical Turbulence Generators for Testing Astronomical Adaptive Optics Systems: A Review and Designer Guide,” PASP 118, 1205-1224, (2006)
[21] Andreas Bazzon , Daniel Gisler , Ronald Roelfsema , Hans M. Schmid , Johan Pragt , Eddy Elswijk , Menno de Haan , Mark Downing , Bernardo Salasnich , Alexey Pavlov , Jean-Luc Beuzit , Kjetil Dohlen ,David Mouillet , François Wildi, “SPHERE / ZIMPOL: characterization of the FLC polarization modulator,” Proc. SPIE 8446, (2012)
[22] Carbillet, M., Boccaletti, A., Thalmann, C., Fusco, T., Vigan, A., Mouillet, D., and Dohlen, K., “The software package SPHERE: a numerical tool for end-to-end simulations of the VLT instrument SPHERE,” Proc. Spie 7015, (2008)
[23] Thalmann, Christian, Schmid, Hans M., Boccaletti, Anthony, Mouillet, David, Dohlen, Kjetil, Roelfsema, Ronald, Carbillet, Marcel, Gisler, Daniel, Beuzit, Jean-Luc, Feldt, Markus, Gratton, Raffaele, Joos, Franco, Keller, Christoph U., Kragt, Jan, Pragt, Johan H., Puget, Pascal, Rigal, Florence, Snik, Frans, Waters, Rens, Wildi, François, “SPHERE ZIMPOL: overview and performance simulation,” Proc. SPIE 7014, 70143F, (2008)

[24] Ronald Roelfsema , Daniel Gisler , Johan Pragt , Hans Martin Schmid , Andreas Bazzon , Carsten Dominik , Andrea Baruffolo , Jean-Luc Beuzit , Julien Charton , Kjetil Dohlen , Mark Downing , Eddy Elswijk , Markus Feldt , Menno de Haan , Norbert Hubin , Markus Kasper , Christoph Keller , Jean-Louis Lizon , David Mouillet , Alexey Pavlov , Pascal Puget , Sylvain Rochat , Bernardo Salasnich , Peter Steiner , Christian Thalmann , Rens Waters , François Wildi, "The ZIMPOL high contrast imaging polarimeter for SPHERE: sub-system test results," Proc. SPIE 8151, (2011)
[25] M. de Juan Ovelar ; S. Diamantopoulou ; R. Roelfsema ; T. van Werkhoven ; F. Snik ; Johan Pragt and C. Keller, Proc. SPIE, 844912 (2012)
[26] D. K. Aitken and J. H. Hough, "Spectral Modulation, or Ripple, in Retardation Plates for Linear and Circular Polarization," Pub. Astron. Soc. Pacific 113, pp. 1300–1305 (2001)
[27] F. Goos and H. H¨anchen, Ann. Phys. 1, 333 (1947)
[28] F. I. Fedorov, Dokl. Akad. Nauk SSSR 105, 465 (1955)
[29] A. Aiello, M. Merano, and J. P. Woerdman, Duality between spatial and angular shift in optical reflection, Phys. Rev. A 80, (2009)
[30] M. Merano, N. Hermosa, J. P. Woerdman, and A. Aiello, How orbital angular momentum affects beam shifts in optical reflection , Phys. Rev. A 82 (2010)
[31] Marois, C., Lafreni`ere, D., Doyon, R., Macintosh, B., and Nadeau, D., "Angular Differential Imaging: A Powerful High-Contrast Imaging Technique," The Astrophysical Journal 641, 556–564 (2006)